
Optical and Plasma Smoothing of Laser Imprinting in Targets Driven by Lasers with SSD Bandwidths up to 1 THz

Introduction

A key issue for inertial confinement fusion (ICF)^{1–3} is the Rayleigh–Taylor (RT) hydrodynamic instability.^{4,5} In direct-drive ICF, nonuniformities in the drive laser produce pressure variations that “imprint” perturbations into the target. Unstable RT growth can amplify these perturbations, resulting in sufficient distortion of the target shell to degrade implosion performance. As coronal plasma is formed around the target, a region of thermal conduction is produced where nonuniform energy deposition can be thermally smoothed^{6–8} before perturbations reach the ablation surface. A mode of laser nonuniformity couples to (or seeds) a mode of hydrodynamic instability up to the time that sufficient plasma smoothing occurs, and then imprinting ceases.⁸ The time to produce this plasma and decouple the laser nonuniformities from the unstable ablation region depends on the perturbation wavelength and the energy deposition rate, i.e., the laser pulse shape. Fast-rising pulses produce plasma more rapidly than slow-rising pulses and therefore cause imprinting over shorter times.⁹ During the time that this plasma evolves, nonuniformities in the drive must be minimized. To do so, many ICF target designs employ laser-beam-smoothing techniques,¹⁰ most of which are time dependent. These techniques are quite effective and have produced marked improvements in the performance of direct-drive targets.¹¹

As a result of these smoothing effects, the amount of imprint experienced by a target depends on the temporal behavior of both the laser uniformity and the plasma evolution. This article describes measurements of the effect of beam smoothing and pulse shape on imprinting, and the results are used to demonstrate the dependence of imprinting on the plasma formation rate. It extends the measurements described in Ref. 9 to the higher smoothing rates of 1-THz smoothing by spectral dispersion (SSD).¹⁰

Laser imprinting begins when nonuniformities in the laser produce variations in the initial pressure, launching nonuniform shocks into the target. These shocks produce velocity perturbations in the target that distort the shock and ablation

fronts. (Regions of higher intensity produce stronger shocks that propagate faster than those driven at lower intensities.) These distortions create lateral mass flow in the shock-compressed material that in turn creates differential pressures that perturb the acceleration profile at the ablation surface. The RT instability exponentially amplifies these acceleration and velocity perturbations, producing additional mass perturbations in the target. (This redistribution of mass can be responsible for degrading the target performance and is observable in many experiments.) In addition to the above, effects such as dielectric breakdown in the target and laser filamentation¹² may create target perturbations that can seed the RT instability.

As the interaction proceeds, more plasma is formed and the laser light is absorbed at increasing distances from the ablation surface. The nonuniformities in intensity continue to drive acceleration perturbations at the ablation front, but thermal smoothing in the intervening plasma (between the absorption and ablation regions) reduces the magnitude of the pressure variations that reach the ablation surface. Eventually, the size of this conduction zone is sufficient to completely smooth the pressure perturbations, and imprinting stops. The calculated condition for the cessation of imprinting is⁸

$$kd_c \sim 2, \quad (1)$$

where k is the wave number of the imprinted perturbation and d_c is the average distance between the absorption region and the ablation surface.¹³ In this article, the effect of the plasma formation rate and beam smoothing on imprinting is experimentally studied and found to be in good agreement with the condition of Eq. (1).

Experiments on the OMEGA laser system¹⁴ measured an equivalent surface roughness of imprinting in planar targets using the growth of preimposed modulations for calibration.⁹ This surface roughness is defined as the mass perturbation that produces similar resultant amplitudes after the linear RT growth phase.¹⁵ Using this measure, the imprinting produced by different temporal pulse shapes and beam-smoothing tech-

niques is compared. Rapidly rising (~ 100 ps/decade) pulses produce less imprint than slowly rising pulses (~ 2.5 -ns rise time) when no temporal beam smoothing is employed. Furthermore, the effect of SSD is less pronounced for these rapid-rise pulses. These are consistent with plasma smoothing⁶⁻⁸ by thermal conduction and the intensity-dependent rate of plasma production.⁹

Simulations^{15,16} that investigated imprinting have indicated that, for a given laser wavelength, the imprint efficiency (equivalent imprint level per fractional laser nonuniformity) depends linearly on the drive nonuniformity (i.e., $\delta m \propto \delta I/I$) for the intensities relevant to direct-drive ICF. The duration of imprinting, however, depends on the time required to produce a sufficiently sized plasma [Eq. (1)] to completely smooth pressure variations created by laser nonuniformities. As the thermal conduction region grows, longer wavelengths can be smoothed; thus, for each wavelength the duration of laser imprinting (and therefore its total magnitude) depends on the time required to develop a sufficiently large conduction zone. The plasma formation rate therefore affects the wavelength dispersion of imprinting. For a given wavelength of interest, imprinting ultimately ceases when the conduction region grows to a sizable fraction of the wavelength, satisfying Eq. (1). Thus, in order to reduce imprinting, it is also important that significant optical beam smoothing occurs while this plasma is forming. The experiments described below demonstrate the interplay between these two effects.

Experiments

In these experiments, six overlapping UV OMEGA beams irradiated 20- μm -thick CH ($\rho = 1.05$ g/cm³) targets with preimposed modulations at 30- and 60- μm wavelengths. These wavelengths correspond to ℓ modes of 50 and 100 on millimeter-sized targets, which are important for direct-drive ICF on OMEGA. Experiments were performed with two laser temporal pulse shapes: a 3-ns square pulse and a 2.5-ns ramp pulse. The square pulse had a rise time of 100 ps per decade of intensity and an intensity of 2×10^{14} W/cm². The ramp pulse rose linearly from $\sim 10^{13}$ to 2.5×10^{14} W/cm² in 2.5 ns after a 100-ps rise to $\sim 10^{13}$ W/cm². For each pulse shape, experiments were performed with and without single-cycle, 2-D SSD beam smoothing at 0.2- and 1.0-THz bandwidths with modulation frequencies of 3×3 GHz and 1.6×11 GHz, respectively. In some cases, polarization smoothing (PS)¹⁷ was added by using wedged birefringent plates.¹⁸

The driven targets were radiographed with x rays produced by a uranium backlighter irradiated at 2×10^{14} W/cm². X rays

transmitted through the target and a 3- μm -thick Al blast shield were imaged by a framing camera with 8- μm pinholes filtered with 20 μm of Be and 6 μm of Al.¹⁹ This filtration provided highest sensitivity at 1.3 keV and a resolution of at least 12 μm .

Since the initial perturbations produced by the laser are quite small, it is difficult to directly measure laser imprint. Measurements often rely on RT growth to produce detectable modulations in the target areal density. Relying on this nonlinear process as an “amplifier” makes it difficult to determine the initial amplitude of the seed, i.e., the amplitude of imprinting. The spectrum of laser nonuniformities is determined by the interference produced by the distributed phase plates (DPP’s)²⁰ and the smoothing produced by SSD. These spectra were measured for a variety of conditions.^{18,21} For the DPP-only case, the power spectrum of nonuniformities peaks at about 6 μm . SSD begins smoothing the shortest wavelengths, almost immediately (~ 25 ps) producing a spectrum that first flattens, then monotonically falls with frequency. These nonuniformities produce target perturbations that evolve due to dispersion in the RT growth and saturation mechanisms. As a result, the perturbation spectra for the various uniformity conditions are similar because the competing effects preferentially amplify the mid-frequencies (i.e., wavelengths from ~ 20 to 100 μm). The primary difference is the amplitude at a given time. Smoother irradiation profiles eventually produce features similar (albeit at later times) to those with higher irradiation nonuniformities. This evolution was shown for various uniformities in Refs. 18 and 22 and discussed at length in Ref. 23. As the spectra evolve, their peak moves to longer wavelengths. For these measurement times the spectral peak typically reaches 30 μm but seldom reaches 60 μm . These wavelengths are therefore of great interest because they can be most damaging to the target.

Low-amplitude, single-mode, preimposed target perturbations (at 30 and 60 μm) were used as a “control” for calibration, from which the initial amplitude of laser imprinting was determined. The basis of this calibration is that, in the linear regime of RT instability, imprinted perturbations grow at the same rate as preimposed modulations.^{9,15,24} Although imprinting also produces velocity and acceleration perturbations, it is useful to assign it an equivalent surface roughness (mass modulation) to imprinting.¹⁵

Imprint was measured in this work by the method illustrated in Fig. 84.1(a), which shows a plot of the amplitude of single-mode target perturbations predicted by the 2-D code *ORCHID*.²⁵ The green curve shows the amplitude evolution

in a target having a 60- μm , single-mode mass perturbation and driven with a spatially perfect laser. The blue curve shows a similar evolution in an initially perfect target (no perturbations) driven by a laser having a single-mode intensity modulation (again with 60- μm wavelength). The blue curve starts at zero amplitude and rises as imprinting begins. At ~ 400 ps, RT growth begins and the evolution of imprint amplitude is parallel to the green curve. The RT instability amplifies both perturbations, imposed or imprinted, in the same manner. The equivalent surface roughness of imprinting can be deduced by extrapolating (dashed curve) the temporal evolution of the imprinted amplitudes (blue curve) back to $t = 0$ using the behavior of the preimposed mode (green curve). In the linear regime, modes of the same wavelength grow at the same rate, and the ratio of amplitudes for these two modes remains constant. Thus, an equivalent initial amplitude for imprinting can be deduced by comparing (after some RT growth) the amplitude of the imprinted mode to a preimposed mode of known initial value. Figure 84.1(b) shows the result of an experiment²³ where a target with a preimposed 60- μm perturbation was driven by a laser with 0.2-THz SSD without polarization smoothing. The upper two curves show the amplitude of the imposed modulations in two different experiments: one with an initial amplitude of 1250 \AA and the other with 500 \AA . The lower curve is the amplitude of the imprinted modes (at the same wavelength) for six different experiments. All experiments were performed under similar laser and target conditions.^{23,26} The points at the lower left have large error bars because the signal is very near the noise level.

Since the imposed and imprinted perturbations grow at the same rate, the upper two curves in Fig. 84.1(b) are parallel to the lower curve. The ratio of the amplitudes for the two

preimposed modes (initial amplitudes of 1250 \AA and 500 \AA) is constant and equal to their ratio at $t = 0$, showing that the RT growth is in the linear regime. This method requires that, for the modes of interest, the RT instability remain in the linear regime and that they experience no saturation or nonlinear effects.²⁷ Saturation of RT growth is discussed at length in Refs. 23 and 26, where it was shown that at $\lambda = 60 \mu\text{m}$, both the single-mode and the imprinted perturbations behaved linearly for the experimental conditions and observation times described in this article. For this experiment the 30- μm -wavelength imprinting data was measured before the onset of its saturation as observed in Refs. 23 and 26.

The amplitude of the equivalent surface roughness for a specific wave number is defined as¹⁵

$$A_{\text{eq}}(k, 0) = [A_{\text{imprint}}(k, t) / A_{\text{pre}}(k, t)] A_{\text{pre}}(k, 0), \quad (2)$$

where $A_{\text{imprint}}(k, t)$ is the measured amplitude of the imprinted features, $A_{\text{pre}}(k, t)$ is the measured amplitude of the preimposed modulation, and $A_{\text{pre}}(0)$ is the known initial amplitude of the preimposed modulation. A measure of imprint efficiency,¹⁵ which can be readily compared to simulations, is $\eta_i(k) = A_{\text{eq}}(k, 0) / (\delta I / I)$, where $\delta I / I$ is the measured fractional irradiation nonuniformity at the same wavelength.

The amplitudes of the perturbations are obtained by Fourier analysis of the x-ray radiographed images.¹⁹ The Fourier amplitude of the imprinted features at a given wavelength is the rms of all mode amplitudes at that wavelength, i.e., those modes at a given radius (centered at zero spatial frequency) in spatial-frequency space (the contribution of the preimposed

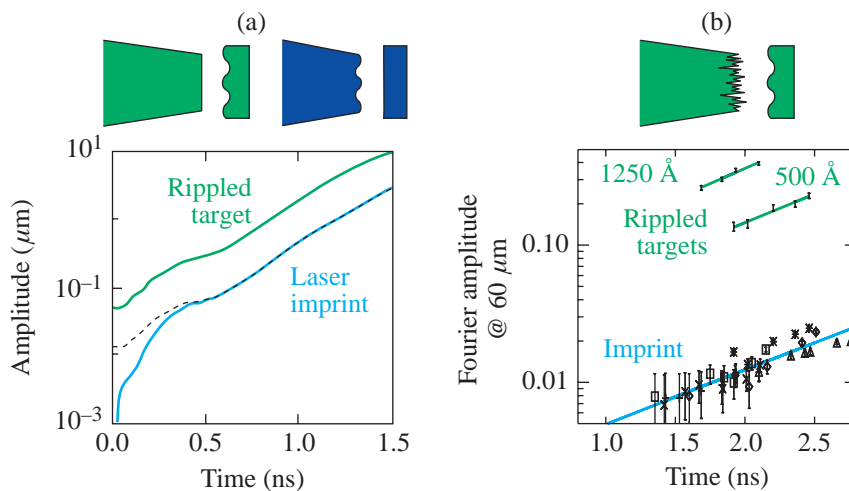


Figure 84.1

Derivation of equivalent surface finish. (a) Simulations of the perturbation amplitude evolution: The green curve is a 60- μm , single-mode mass perturbation driven with a spatially perfect laser. The blue curve shows the similar evolution in an initially perfect target (no perturbations) driven by a laser having a 60- μm , single-mode intensity modulation. The equivalent surface finish is defined as the point where the dashed curve intercepts $t = 0$. (b) Experimental results showing the measured amplitudes (optical depth) for imprinted (lower set) and imposed modulations (upper two sets). All are at 60- μm wavelength.

E9502

modulation is not included). The features of interest at $30\ \mu\text{m}$ and $60\ \mu\text{m}$ are easily observed by the camera, which has $\sim 15\text{-}\mu\text{m}$ resolution.

The preimposed single-mode modulations appear as localized features along a single axis in the Fourier plane and at the spatial frequency of their modulation. The time-dependent amplitude of the preimposed mode is obtained by subtracting (in quadrature) the rms amplitude of the imprinted modes at the same time. The analysis box is $\sim 300\ \mu\text{m}$ in the target plane; thus, in Fourier space, the pixel size is $\sim 3.3\ \text{mm}^{-1}$. (The box size is optimized to ensure that all the power in the preimposed mode is contained in a single pixel in each Fourier half-plane.)

For these experiments a variety of beam-smoothing techniques were used. A single-beam laser with a DPP and no SSD provides a static speckle pattern with $\sim 80\%$ to 100% nonuniformity in wavelengths from $2\ \mu\text{m}$ to $250\ \mu\text{m}$.²¹ The speckle results from the interference of many beamlets produced by diffraction in the DPP optic. The speckle pattern is statistical in nature with a sufficiently short correlation length that multiple overlapped beams can be treated as statistically independent patterns. Thus six-beam irradiation reduces this nonuniformity to $\sqrt{6}$ times lower than the single-beam value. Additional beam smoothing is provided by SSD, which, by introducing bandwidth onto the laser, produces a statistically independent speckle pattern every $\Delta t = t_c$, where $t_c \sim 1/\Delta\nu$ is the correlation time and $\Delta\nu$ is the UV laser bandwidth.¹⁰ SSD does not reduce nonuniformities instantaneously, rather the time-averaged rms uniformity is reduced by $\sqrt{t_c/\langle t \rangle}$, where $\langle t \rangle$ is the averaging time. Thus, the drive uniformity is time dependent and varies with the amount of bandwidth applied to the laser. These experiments were performed with one of two laser bandwidths, either $\Delta\nu = 0.2\ \text{THz}_{\text{UV}}$ or $1.0\ \text{THz}_{\text{UV}}$. (All experiments with SSD used two-dimensional SSD.) In the former case the IR bandwidths were $1.25\ \text{\AA} \times 1.75\ \text{\AA}$ and in the latter case $1.6\ \text{\AA} \times 11\ \text{\AA}$. In some cases, polarization smoothing (PS) using birefringent wedges¹⁸ was added to the drive beams. Polarization smoothing provides an instantaneous $\sqrt{2}$ reduction in nonuniformity by dividing each beam into two orthogonal polarizations that are separated by $80\ \mu\text{m}$ in the target plane.¹⁸

Figure 84.2 shows the equivalent surface roughness (in μm) of imprinting measured at $60\text{-}\mu\text{m}$ wavelength for a series of shots that used a 3-ns square pulse with four different smoothing conditions (all with similar drive intensities). The temporal axis is the time at which each measurement was taken. These data separate into distinct sets associated with

each uniformity condition and are constant in time. Both these observations are expected and confirm the utility of this technique. When the growth of the imprinted features is in the linear regime, their amplitude should remain a constant fraction of that of the preimposed mode, leading to a constant inferred surface roughness. This quantity's dependence on the initial uniformity produced by the various beam-smoothing techniques indicates the sensitivity of the method. For example, the addition of polarization smoothing (diamonds) to the 0.2-THz SSD experiments (blue squares) reduced the equivalent surface roughness by the expected factor of $\sqrt{2}$. Similarly, the increase in the SSD bandwidth from 0.2 (blue squares) to 1.0 (x's) THz without polarization smoothing reduced the equivalent surface roughness by ~ 0.60 . This is the reduction expected from models of the optical smoothing by SSD (see below). The results for all conditions are listed in Table 84.I.

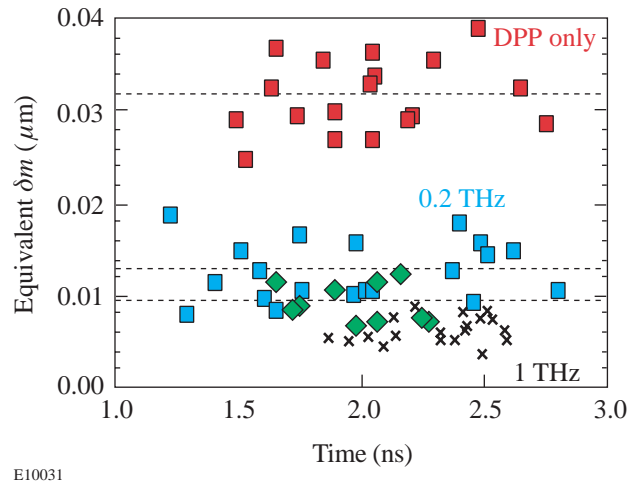


Figure 84.2

The equivalent surface roughness (in μm) at $60\text{-}\mu\text{m}$ wavelength derived from planar targets driven by laser beams having a 3-ns square pulse and four types of beam smoothing applied: DPP only (red squares), DPP + 0.2-THz SSD (blue squares), DPP + 0.2-THz SSD + PS (diamonds), and DPP + 1-THz SSD (x's). The data segregate according to the laser nonuniformity with the total amount of imprinting decreasing with increased beam smoothing.⁹

The effect of pulse shape on imprinting was studied by repeating these measurements with a slowly rising pulse, i.e., with a $\sim 2.5\text{-ns}$ rise to the maximum intensity. Figure 84.3 shows the equivalent surface roughness as a function of time for the two pulse shapes, each with and without 0.2-THz SSD. Again the data group according to laser conditions (pulse shape or SSD) and exhibit an approximately constant value over a considerable time.

These data show that without SSD the ramp pulse (red triangles) produces about 50% more imprinting (rougher equivalent surface) than the square pulse (red squares). They also indicate that 0.2-THz SSD produces a greater reduction of imprinting ($\sim 2.5\times$) on the ramp pulse (blue triangles) than for the factor of 2.2 observed for the square pulse (blue squares). Similar experiments were performed using preimposed modulations with $\lambda = 30 \mu\text{m}$.

The imprint efficiency was calculated for the experiments without SSD using the single-beam irradiation nonuniformities reported in Ref. 21. The uniformity results were scaled by the

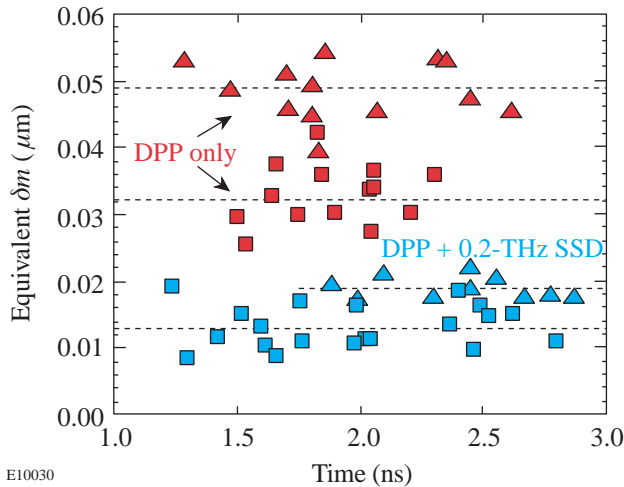


Figure 84.3 The deduced equivalent surface roughness of the imprinted features (at $60 \mu\text{m}$) for two pulse shapes: 3-ns square (squares) and ramp (triangles). These data show that for the same laser nonuniformity, a ramp pulse produces more imprinting. The blue and red symbols correspond, respectively, to each of the pulses with and without 2-D SSD. They indicate that the effect of SSD is greater for the ramp pulse.⁹

differences in analysis boxes between the x-ray radiography ($L = 300 \mu\text{m}$; $\Delta k = 0.021 \mu\text{m}^{-1}$) and the optical experiments ($L = 440 \mu\text{m}$; $\Delta k = 0.0143 \mu\text{m}^{-1}$). In addition, the values obtained in Ref. 21 were reduced by $\sqrt{6}$ since these experiments utilized six overlapped beams. Thus, $\delta I/I$ was 0.0068 for $30 \mu\text{m}$ and 0.0049 for $60 \mu\text{m}$. Lastly, a factor of 2 was included to relate the complex amplitude for $\delta I/I$ to the equivalent surface roughness, which was normalized using a real (cosine) function. The measured imprint efficiencies are shown in Table 84.I. Since the SSD produces time-varying uniformity, it is difficult to assign a single number to the uniformity; therefore, the imprint efficiency is not quoted for those cases. The effect of SSD will be discussed below.

As discussed above, the duration of imprinting depends on the time required to produce sufficient plasma atmosphere to enable smoothing. As a result, the ramp pulse imprints for a longer duration than the square pulse because it delivers energy at a slower rate and therefore generates the smoothing plasma more slowly. Thus the ramp pulse will imprint for a longer duration, leading to a higher equivalent roughness. The imprint efficiencies measured here are lower, as expected, than those observed by Glendinning *et al.*^{24,28} using an even slower rise and lower-intensity ramp pulse.

Simulations of Imprint and Plasma Smoothing

The experiments were simulated with the 2-D hydrodynamics code *ORCHID* to determine the predicted imprint efficiency and the effects of plasma smoothing. The imprint efficiencies were calculated by imposing a single-mode nonuniformity in the laser irradiation. The evolution of the resulting perturbations was compared to that of preimposed mass perturbations at the same wavelength. The experimental temporal pulse shapes were used in the simulations. The simulation results shown in Table 84.I are in reasonable

Table 84.I: Equivalent surface roughness and imprint efficiency for various conditions.

Pulse-Shape Uniformity	Equivalent Surface Roughness (μm)		Imprint Efficiency: $(\delta m/\rho)/(\delta I/I)$ (μm)			
			Experiment		Simulation	
	$60 \mu\text{m}$	$30 \mu\text{m}$	$60 \mu\text{m}$	$30 \mu\text{m}$	$60 \mu\text{m}$	$30 \mu\text{m}$
Square (no SSD)	0.032 ± 0.005	0.022 ± 0.004	3.3 ± 0.4	1.6 ± 0.3	1.7	1.1
Ramp (no SSD)	0.049 ± 0.008	0.023 ± 0.005	5.0 ± 0.6	1.7 ± 0.4	3.1	2.3
Square (0.2-THz SSD)	0.013 ± 0.003	0.010 ± 0.003				
Ramp (0.2-THz SSD)	0.017 ± 0.005	0.011 ± 0.004				
Square (1-THz SSD)	0.009 ± 0.0018	0.0044 ± 0.0015				
Ramp (1-THz SSD)	0.0105 ± 0.0022	0.0054 ± 0.0019				

agreement with the measured values. Similar imprint efficiencies were calculated with the 2-D hydrodynamics code *LEEOR*.²⁹ The 2-D simulations underestimate the imprint efficiency at $60\ \mu\text{m}$, similar to the observations of Glendinning *et al.*^{24,28} For the $30\text{-}\mu\text{m}$ perturbations, the simulations also underestimate the square-pulse data but overestimate the ramp-pulse data.

The inherent real surface roughness of these foils (transverse to the imposed modulations) was measured to be less than 1% of the imposed mode and, therefore, did not contribute significantly to the error in the measurements of either the imprinted or the imposed modes. The measured signal for the preimposed mode also has a contribution from the imprinted signal at that distinct mode. Since the relative phase of these two signals is arbitrary, the resultant signal can vary significantly when the imprint is a sizable fraction of the preimposed mode. To minimize this effect, the imprinted modes were kept below 30% of the imposed mode by increasing the amplitude of the imposed modes on shots without SSD. Most experiments were performed with the imprint between 0.1 and 0.25 of the imposed mode. This represented a trade-off between the noises from either too low a signal in the imprinted modes or that affecting determination of the imposed mode, while keeping both signals below the saturation limits.

The effect of plasma formation rate on thermal smoothing of nonuniform energy deposition was investigated using *ORCHID*. Figure 84.4 shows the calculated amplitude of pressure perturbations (solid curves) at the ablation surface as

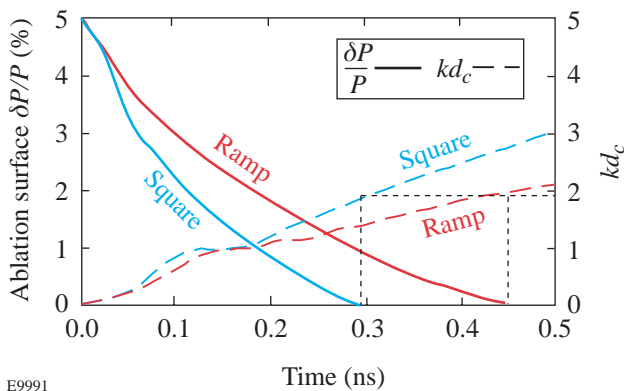


Figure 84.4

The calculated amplitude of $60\text{-}\mu\text{m}$ perturbations (solid curves) in the pressure at the ablation surface as a function of time. The size of the conduction zone (dashed curves) as a function of time in CH targets driven by the square and ramp pulses. These graphs show that, for $60\text{-}\mu\text{m}$ perturbations, decoupling occurs at 290 ps for the square pulse and 450 ps for the ramp pulse.⁹

a function of time for two cases: a ramp pulse and a square pulse, both without SSD. In these simulations a static $60\text{-}\mu\text{m}$ -wavelength, 5% spatial-intensity modulation was imposed on the irradiation profile. The pressure perturbations that reach the ablation surface diminish as the plasma expands. Note that for the ramp pulse, the smoothing rate is slower and the perturbations persist for a longer period. The temporal evolution (dashed curves) of the normalized conduction zone (kd_c) for the two pulse shapes is also shown. This is defined as the distance between the ablation surface and the mean of the energy deposition profile as weighted by a diffusion length e^{-kz} and is normalized to the wave number.¹³ (The energy deposition profile must also be accounted for since considerable smoothing can take place in the plasma region outside the critical surface.) Imprinting ceases when pressure perturbations at the ablation surface are reduced to negligible levels. Figure 84.4 shows that for both pulse shapes this occurs when $kd_c \sim 2$, providing a measure of the decoupling time for the case of constant uniformity (no SSD). This analysis has also been applied to other wavelengths and both pulse shapes, and found to confirm that $kd_c \sim 2$ is the applicable condition. Figure 84.5 shows the simulations of the normalized smoothing length (kd_c) as a function of time for the square (dashed) and ramp (solid) pulses for three wavelengths: 30, 60, and $120\ \mu\text{m}$. The solid points indicated the time at which the modulations in ablation pressure diminish to zero for each case. This occurs for $kd_c \sim 2$ for all six cases. As the plasma evolves, shorter wavelengths are smoothed sooner than longer wavelengths; this in part determines the dispersion in wavelength of the imprint efficiency. Thus, for the broad spectrum of laser

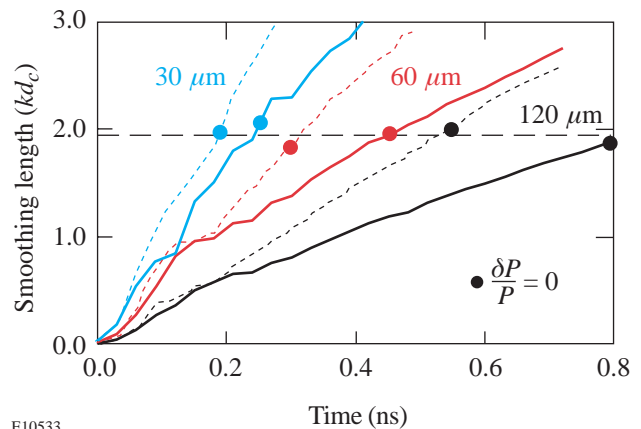


Figure 84.5

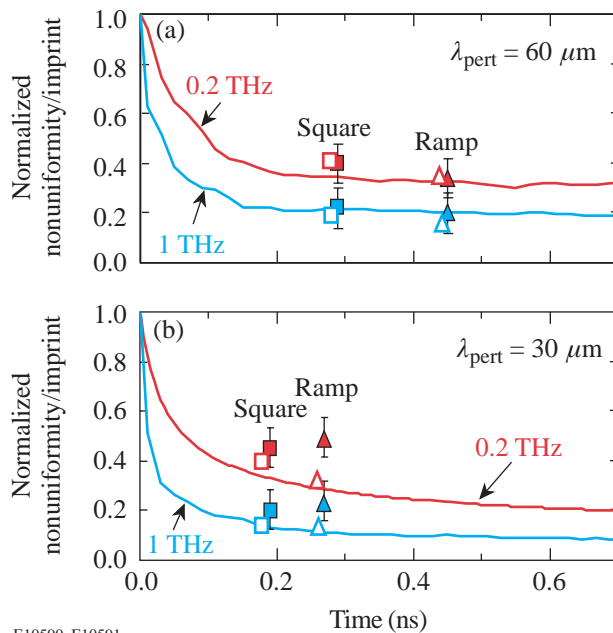
Simulations of the normalized smoothing length (kd_c) versus time for square (dashed) and ramp (solid) pulses. The points indicate the time at which the modulations in ablation pressure diminish to zero. Perturbations with wavelengths of 30, 60, and $120\ \mu\text{m}$ are all smoothed when $kd_c \sim 2$.

nonuniformities present in laser speckle, the short-wavelength modes are smoothed first. These modes also have faster growth rates and experience saturation sooner than longer-wavelength modes. In contrast, the longer-wavelength modes are smoothed less, but also grow at slower rates. As a result, intermediate wavelengths (ℓ modes of 50 to 100 on millimeter-sized targets) become dominant and, therefore, are of most concern for target stability. The calculated decoupling times for 60- μm wavelengths were found to be 290 and 450 ps for the square and ramp pulses, respectively. For 30- μm wavelengths, the respective times were 190 and 270 ps.

Decoupling and the Dynamics of Smoothing

Plasma smoothing and decoupling of imprinted perturbations are confirmed experimentally by analyzing experiments with time-dependent beam smoothing. By matching the observed reduction of imprinting to the smoothing rate of SSD, the effect of thermal smoothing by the plasma atmosphere is observed. Figure 84.6 shows the imprint reduction [at (a) 60- μm and (b) 30- μm wavelengths] as a function of time for SSD bandwidths of 0.2 (red solid points) and 1.0 (blue solid points) THz_{UV}. In each, the curves are the irradiation non-

uniformity (normalized to that at $t = 0$) predicted by an optical model²¹ (basically a $1/\sqrt{t\Delta\nu}$ dependence). The points are the measurements of the reduction in imprinting due to SSD. This reduction is calculated by normalizing the SSD data to measurements without SSD. Reference 21 demonstrated that the optical model accurately predicts the smoothing rate and the ultimate uniformity achieved with 0.2-THz SSD (red curve). It is expected that it represents the performance of 1.0 THz (blue curve) as well. The imprint data are plotted at the calculated decoupling times described above. The square-pulse data (squares) are shown for 0.2 THz (red points) and 1.0 THz (blue points). The ramp-pulse data (triangles) are similarly coded for SSD. The predictions (open symbols) are shown slightly displaced in time for clarity. Figure 84.6 shows that (1) for 60 μm the calculated decoupling times are consistent with the optical data and (2) the hydrocode models the effect of SSD and the plasma production rate (pulse shape) quite well. The 30- μm data for the ramp pulse are above both the optical smoothing rate and the hydrocode results, i.e., the reductions are less than expected. This may be caused by the imprinting measurement for the no-SSD, 30- μm case (denominator for reduction calculation) being too low. A possible mechanism for error in the measured imprint is the onset of saturation in the imprinted (3-D) modes that has not yet affected the preimposed (2-D) modes. Reference 23 showed that for these conditions the 30- μm perturbations can experience saturation if the amplitudes are high enough. Furthermore, the ramp pulse, because of its late decoupling time, imprints more readily and therefore would be most susceptible to saturation. Unfortunately, the spread in data does not allow its temporal trend to be discerned with precision and saturation cannot be easily detected.



E10590, E10591

Figure 84.6

The normalized nonuniformity [(a) for 60 μm and (b) for 30 μm] as predicted by the optical model (curves) with the measured reductions in imprint for 0.2 THz (solid points) and 1 THz (shaded points) for square (squares) and ramp (triangles) pulse shapes. The predictions by *ORCHID* are shown as open points (similarly identified).

Conclusion

Using preimposed modulations on planar targets to calibrate imprinting amplitudes, this work has confirmed imprinting's expected dependence on drive-laser nonuniformity, showing the utility of the equivalent-surface technique. It has demonstrated that imprinting depends on the temporal shape of the drive laser. This occurs because thermal smoothing in the coronal plasma ultimately limits the duration of imprinting and therefore its total amplitude. Once there is sufficient plasma, the pressure perturbations no longer reach the unstable ablation surface and imprinting stops. Steeply rising pulses produce plasma more rapidly than slowly rising pulses and therefore produce less imprinting. The simulations of the static cases (DPP's only) show behavior that is consistent with the decoupling times predicted for these conditions. Moreover, using the dynamic case of 2-D SSD, the improvements in uniformity inferred by measuring imprint are consis-

tent with both the measured rate of smoothing by SSD and the decoupling times predicted by the hydrocodes; they also verify the predictions of Eq. (1). The increase in laser bandwidth to 1 THz has produced reductions in the imprint level that agree with expected performance. These results provide confidence in our ability to model and control imprinting in direct-drive ICF targets.

ACKNOWLEDGMENT

This work was supported by the U.S. Department of Energy Office of Inertial Confinement Fusion under Cooperative Agreement No. DE-FC03-92SF19460, the University of Rochester, and the New York State Energy Research and Development Authority. The support of DOE does not constitute an endorsement by DOE of the views expressed in this article.

REFERENCES

1. J. Nuckolls *et al.*, *Nature* **239**, 139 (1972).
2. J. D. Lindl, *Phys. Plasmas* **2**, 3933 (1995).
3. S. E. Bodner, D. G. Colombant, J. H. Gardner, R. H. Lehmborg, S. P. Obenschain, L. Phillips, A. J. Schmitt, J. D. Sethian, R. L. McCrory, W. Seka, C. P. Verdon, J. P. Knauer, B. B. Afeyan, and H. T. Powell, *Phys. Plasmas* **5**, 1901 (1998).
4. Lord Rayleigh, *Proc. London Math Soc.* **XIV**, 170 (1883).
5. G. Taylor, *Proc. R. Soc. London Ser. A* **201**, 192 (1950).
6. K. A. Brueckner and S. Jorna, *Rev. Mod. Phys.* **46**, 325 (1974).
7. S. E. Bodner, *Phys. Rev. Lett.* **33**, 761 (1974).
8. V. N. Goncharov, S. Skupsky, T. R. Boehly, J. P. Knauer, P. McKenty, V. A. Smalyuk, R. P. J. Town, O. V. Gotchev, R. Betti, and D. D. Meyerhofer, *Phys. Plasmas* **7**, 2062 (2000).
9. T. R. Boehly, V. N. Goncharov, O. Gotchev, J. P. Knauer, D. D. Meyerhofer, D. Oron, S. P. Regan, Y. Srebro, W. Seka, D. Shvarts, S. Skupsky, and V. A. Smalyuk, "The Effect of Plasma Formation Rate and Beam Smoothing on Laser Imprinting," submitted to *Physical Review Letters*.
10. S. Skupsky and R. S. Craxton, *Phys. Plasmas* **6**, 2157 (1999).
11. D. D. Meyerhofer, J. A. Delettrez, R. Epstein, V. Yu. Glebov, R. L. Keck, R. L. McCrory, P. W. McKenty, F. J. Marshall, P. B. Radha, S. P. Regan, W. Seka, S. Skupsky, V. A. Smalyuk, J. M. Soures, C. Stoeckl, R. P. J. Town, B. Yaakobi, R. D. Petrasso, J. A. Frenje, D. G. Hicks, F. H. Séguin, C. K. Li, S. Haan, S. P. Hatchett, N. Izumi, R. Lerche, T. C. Sangster, and T. W. Phillips, "Core Density and Temperature Conditions and Fuel-Pusher Mix in Direct-Drive ICF Implosions," to be published in *Physics of Plasmas*.
12. H. A. Rose and D. F. DuBois, *Phys. Fluids B* **5**, 3337 (1993).
13. H. Azechi *et al.*, *Phys. Plasmas* **4**, 4079 (1997).
14. T. R. Boehly, D. L. Brown, R. S. Craxton, R. L. Keck, J. P. Knauer, J. H. Kelly, T. J. Kessler, S. A. Kumpan, S. J. Loucks, S. A. Letzring, F. J. Marshall, R. L. McCrory, S. F. B. Morse, W. Seka, J. M. Soures, and C. P. Verdon, *Opt. Commun.* **133**, 495 (1997).
15. S. V. Weber, S. G. Glendinning, D. H. Kalantar, M. H. Key, B. A. Remington, J. E. Rothenberg, E. Wolftrum, C. P. Verdon, and J. P. Knauer, *Phys. Plasmas* **4**, 1978 (1997).
16. R. J. Taylor *et al.*, *Phys. Rev. Lett.* **79**, 1861 (1997).
17. Y. Kato, unpublished notes from work at LLE, 1984.
18. T. R. Boehly, V. A. Smalyuk, D. D. Meyerhofer, J. P. Knauer, D. K. Bradley, R. S. Craxton, M. J. Guardalben, S. Skupsky, and T. J. Kessler, *J. Appl. Phys.* **85**, 3444 (1999).
19. V. A. Smalyuk, T. R. Boehly, D. K. Bradley, J. P. Knauer, and D. D. Meyerhofer, *Rev. Sci. Instrum.* **70**, 647 (1999).
20. Y. Lin, T. J. Kessler, and G. N. Lawrence, *Opt. Lett.* **20**, 764 (1995).
21. S. P. Regan, J. A. Marozas, J. H. Kelly, T. R. Boehly, W. R. Donaldson, P. A. Jaanimagi, R. L. Keck, T. J. Kessler, D. D. Meyerhofer, W. Seka, S. Skupsky, and V. A. Smalyuk, *J. Opt. Soc. Am. B* **17**, 1483 (2000).
22. T. R. Boehly, R. L. McCrory, C. P. Verdon, W. Seka, S. J. Loucks, A. Babushkin, R. E. Bahr, R. Boni, D. K. Bradley, R. S. Craxton, J. A. Delettrez, W. R. Donaldson, R. Epstein, D. Harding, P. A. Jaanimagi, S. D. Jacobs, K. Kearney, R. L. Keck, J. H. Kelly, T. J. Kessler, R. L. Kremens, J. P. Knauer, D. J. Lonobile, L. D. Lund, F. J. Marshall, P. W. McKenty, D. D. Meyerhofer, S. F. B. Morse, A. Okishev, S. Papernov, G. Pien, T. Safford, J. D. Schnittman, R. Short, M. J. Shoup III, M. Skeldon, S. Skupsky, A. W. Schmid, V. A. Smalyuk, D. J. Smith, J. M. Soures, M. Wittman, and B. Yaakobi, *Fusion Eng. Des.* **44**, 35 (1999).
23. V. A. Smalyuk, T. R. Boehly, D. K. Bradley, V. N. Goncharov, J. A. Delettrez, J. P. Knauer, D. D. Meyerhofer, D. Oron, D. Shvarts, Y. Srebro, and R. P. J. Town, *Phys. Plasmas* **6**, 4022 (1999).
24. S. G. Glendinning, S. N. Dixit, B. A. Hammel, D. H. Kalantar, M. H. Key, J. D. Kilkenny, J. P. Knauer, D. M. Pennington, B. A. Remington, R. J. Wallace, and S. V. Weber, *Phys. Rev. E* **54**, 4473 (1996).
25. R. L. McCrory and C. P. Verdon, in *Inertial Confinement Fusion*, edited by A. Caruso and E. Sindoni (Editrice Compositori, Bologna, Italy, 1989), pp. 83–124.
26. V. A. Smalyuk, T. R. Boehly, D. K. Bradley, V. N. Goncharov, J. A. Delettrez, J. P. Knauer, D. D. Meyerhofer, D. Oron, and D. Shvarts, *Phys. Rev. Lett.* **81**, 5342 (1998).
27. S. W. Haan, *Phys. Rev. A* **39**, 5812 (1989).
28. S. G. Glendinning, S. N. Dixit, B. A. Hammel, D. H. Kalantar, M. H. Key, J. D. Kilkenny, J. P. Knauer, D. M. Pennington, B. A. Remington, J. Rothenberg, R. J. Wallace, and S. V. Weber, *Phys. Rev. Lett.* **80**, 1904 (1998).
29. D. Shvarts, U. Alon, D. Ofer, R. L. McCrory, and C. P. Verdon, *Phys. Plasmas* **2**, 2465 (1995).